Acta Crystallographica Section B
Structural Science
ISSN 0108-7681

Structure of the new mineral sarrabusite, $Pb_5CuCl_4(SeO_3)_4$, solved by manual electron-diffraction tomography

Mauro Gemmi,[a,b]* Italo Campostrini,[c] Francesco Demartin,[c] Tatiana E. Gorelik[d] and Carlo Maria Gramaccioli[c]

[a]Center for Nanotechnlogy Innovation@NEST, Istituto Italiano di Tecnologia, Piazza S. Silvestro 12, I-56127 Pisa, Italy, [b]Dipartimento di Scienze della Terra, Università degli Studi di Milano, Via S. Botticelli 23, I-20133 Milano, Italy, [c]Dipartimento di Chimica Strutturale e Stereochimica Inorganica, Università degli Studi di Milano, Via G. Venezian 21, I-20133 Milano, Italy, and [d]Institute of Physical Chemistry, Johannes Gutenberg University, Welderweg 11, 55128 Mainz, Germany

Correspondence e-mail: mauro.gemmi@iit.it

Received 24 July 2011
Accepted 7 November 2011

The new mineral sarrabusite $Pb_5CuCl_4(SeO_3)_4$ has been discovered in the Sardinian mine of Baccu Locci, near Villaputzu. It occurs as small lemon–yellow spherical aggregates of tabular crystals (< 10 μm) of less than 100 μm in diameter. The crystal structure has been solved from and refined against electron diffraction of a microcrystal. Data sets have been measured by both a manual and an automated version of the new electron-diffraction tomography technique combined with the precession of the electron beam. The sarrabusite structure is monoclinic and consists of (010) layers of straight chains formed by alternating edge-sharing CuO_4Cl_2 and PbO_8 polyhedra parallel to the *c* axis, which share corners laterally with two zigzag corner-sharing chains of PbO_6Cl_2 and PbO_4Cl_4 bicapped trigonal prisms. These blocks are linked together by SeO_3^{2-} flat-pyramidal groups.

1. Introduction

1.1. A new mineral from Baccu Locci mine

An old lead and arsenic mine is known at Baccu Locci near Villaputzu, in southeastern Sardinia, Italy. The deposit is located in a hydrothermal ore body hosted in Paleozoic 'black shales'. This locality is well known among mineralogists and collectors for the presence of an unusual number of rare secondary minerals, among which are selenites such as chalcomenite, schmiederite, olsacherite and mandarinoite. Of these species, particularly interesting are those also containing chlorides, such as orlandiite, a lead hydrated selenite-chloride $Pb_3Cl_4(SeO_3)\cdot H_2O$ for which Baccu Locci is the type locality, and francisite $Cu_3Bi(SeO_3)_2O_2Cl$, for which this mine is the second occurrence in the world (Campostrini *et al.*, 1999; Campostrini & Gramaccioli, 2001). The remarkable quality of the chalcomenite crystals, which can be up to 2 cm in length, has permitted the first accurate refinement of the crystal structure from natural samples (Pasero & Perchiazzi, 1989). At the same locality, the mineral discussed here (mentioned as 'UK1'; in Campostrini *et al.*, 1999), whose chemical formula was then tentatively assigned as $Pb_4CuCl_3(SeO_3)_3(OH)$, was observed for the first time in association with secondary lead and copper minerals, among which in particular are orlandiite $Pb_3Cl_4(SeO_3)\cdot H_2O$, chalcomenite $CuSeO_3\cdot 2H_2O$, anglesite and pseudoboleite $Pb_{31}Cu_{24}Cl_{62}(OH)_{48}$ (Campostrini *et al.*, 1999). However, owing to the exceedingly small dimensions of the crystals (< 10 μm), which aggregate into small spheres of less than 100 μm in diameter, no structural study could be performed using conventional X-ray diffraction and the nature of this possibly new species remained unknown for more than a decade.

1.2. Electron-diffraction tomography technique

Whenever the crystallite size is around or smaller than 1 μm, as often happens in multiphase samples, the crystal structure can be most easily elucidated using electron diffraction (Zou & Hovmöller, 2008). However, electron-diffraction data are very difficult to interpret beyond the unit-cell determination, mainly because dynamical effects destroy the linear relationships between the scattered intensity and the square modulus of the structure factor (Cowley, 1968; Turner & Cowley, 1969). The precession electron-diffraction technique (PED) first proposed by Vincent & Midgley (1994) enabled crystallographers to make a big step towards kinematical diffraction. In PED a zone-axis pattern is taken while the beam is precessing on a cone surface; therefore, since the crystal is always slightly off a perfect zone-axis orientation, few reflections are simultaneously excited and if the precession angle is large ($\sim 3^\circ$) and the density of diffraction spots is not too high (see Oleynikov *et al.*, 2007), the non-systematic dynamical scattering is strongly reduced. The reduction of the dynamical effects makes the reflection intensities suitable for structure solution. As a consequence, several structure determinations based on PED data have been reported over the last few years (see, for instance, Gjønnes *et al.*, 1998; Gemmi *et al.*, 2003, 2010; Dorset, 2006; Weirich *et al.*, 2006; Own *et al.*, 2006; Boullay *et al.*, 2009; Hadermann *et al.*, 2010; Meshi *et al.*, 2010; White, Moreno & Midgley, 2010; Klein, 2011). In addition, new structure characterization methods based on PED were also developed (Nicolopoulos & Weirich, 2007; Xie *et al.*, 2008; Ji *et al.*, 2009; Morniroli *et al.*, 2010; Portillo *et al.*, 2010). Among these procedures, the introduction of automated diffraction tomography or 'ADT' (Kolb *et al.*, 2007) in connection with PED is very promising, since it practically transforms the results obtained from an electron microscope into those provided by a single-crystal diffractometer (Mugnaioli *et al.*, 2009); such a process was already successfully applied to a number of organic and inorganic crystals (Kolb *et al.*, 2010; Birkel *et al.*, 2010; Jiang *et al.*, 2011), including the mineral charoite (Rozhdestvenskaya *et al.*, 2010).

In the ADT method a series of electron-diffraction patterns are collected sequentially in angular steps (usually 1°), while the crystal is tilted $\pm\alpha_{max}$ around the eucentric axis of the microscope goniometer, where α_{max} is the maximum achievable tilt angle of the microscope holder. The patterns are collected with a quasi-parallel nanobeam 50–100 nm wide, and the unavoidable movement of the crystal after each tilt is accounted for by checking the crystal position in a STEM image. A tracking routine cross-correlates the actual STEM image with the previous one, and shifts the nanobeam back to its original position in the image, in order to obtain a diffraction pattern from the same area. Tilting and tracking routines are combined into a completely automated module. The output of the data collection is a set of diffraction patterns in which each pixel can be transformed into a point in the three-dimensional reciprocal space of the crystal. An *ad hoc* designed software can reconstruct the reciprocal volume, and extract from it the unit-cell parameters and the reflection intensities, which then can be used for *ab initio* structure determination (Kolb *et al.*, 2008). With a tilt step of 1°, empty wedges between single frames of the three-dimensional volume are unavoidable. In principle, a complete filling of reciprocal volume can be achieved, provided a small enough tilt step is used. Practically, collecting a data set with a very small angular step ($< 0.5^\circ$) in an ADT experimental configuration would be a very time-consuming procedure, which may be very critical for electron-beam-sensitive materials. To avoid that in ADT the patterns are collected in precession mode with a semi-cone aperture comparable with the angular step. In this way the precession movement of the beam allows reflection intensities within a certain wedge to be integrated.

Electron-diffraction reflection intensities obtained *via* the combination of ADT with PED are suitable for structure solution for two reasons: they suffer less from dynamical effects since they are collected with the crystal in a random orientation, and they are integrated over the excitation error by precession. This last characteristic has been discovered to be the major factor that makes precessed electron-diffraction intensities independent of the structure-factor phases and therefore directly connected to the squared structure-factor moduli (Sinkler & Marks, 2010; White, Eggeman & Midgley, 2010). In PED, since the Ewald sphere is precessing around the optical axis, it sweeps the reciprocal space at a high angle faster than at a low angle causing the reflection at a high angle to stay in the Bragg condition for less time. There is a formula to correct this effect (Gjønnes, 1997; Gemmi & Nicolopoulos, 2007), which unfortunately starts to be too approximate if the precession angle becomes small, like in the ADT case. At the moment no geometrical correction is applied to the ADT data.

An alternative approach, called rotation methods, from the method developed in the X-ray field by Arndt & Wonnacott (1977), was recently developed by Zhang *et al.*, (2010) by combining the goniometer tilt with a relatively large step ($> 2^\circ$) with fine beam tilt steps in between (0.05°). In this way the reciprocal space is sampled very precisely, each 0.05°, and the dependence of the intensity of each reflection with the excitation error can be studied in detail.

Generally, ADT data implies 'off-zone' electron-diffraction patterns collected from a single-crystal through a tilt around an arbitrary axis. Collection of this kind of data does not necessarily require the automated acquisition module, but can be performed manually in selected area mode (SAED) using conventional TEM mode for imaging. SAED precessed patterns should be taken with the caution of keeping the current in the second condenser lens fixed to a certain value in order to be sure that all the patterns are taken under the same illumination conditions. The position of the SAED diaphragm must be checked after every tilt by going back in normal TEM image mode and re-centring the crystal. It was shown recently that manually collected data are just as good for *ab initio* structure solution as the ADT data (Gorelik *et al.*, 2011), so that even an incommensurately modulated structure could be solved *ab initio* (Palatinus *et al.*, 2011).

Table 1
Chemical composition of sarrabusite obtained at the electron microprobe.

Constituent	wt%	Range	Probe standard
Cl	8.41	8.29–8.49	Phosgenite
PbO	61.26	59.97–62.11	Anglesite
SO_2	0.14	0.12–0.16	Anglesite
CdO	1.44	1.24–1.55	Pure metal
CuO	4.29	4.01–4.41	Pure metal
SeO_2	24.84	23.90–25.91	Pure metal
Less O=Cl	1.90		
Total	98.48		

The structure of the new mineral was solved *ab initio* using direct methods with manually and automatically collected diffraction tomography data. Both structure models obtained from completely different setups were consistent, apart from slight shifts of the light anions.

Both the mineral and the name 'sarrabusite' (from Sarrabus, the Sardinian region of occurrence) have been approved by the IMA Commission on New Minerals, Nomenclature and Classification of the IMA (1997-046a).

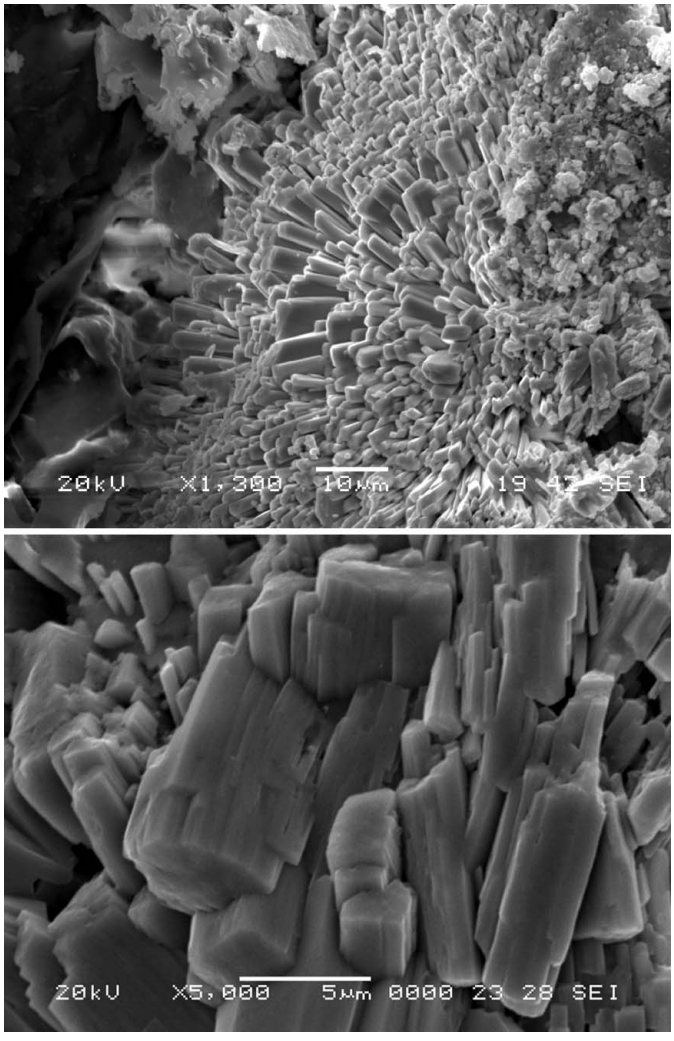

Figure 1
SEM images of two aggregates of sarrabusite crystals.

2. Experimental

Chemical analyses were carried out using an ARL electron microprobe (WDS mode, 15 kV, 15 nA, 15 µm beam diameter). X-ray powder diffraction data were obtained using a Rigaku DMAX-II diffractometer, using monochromated Cu $K\alpha$ radiation.

Conventional transmission electron microscopy and manually collected diffraction tomography were carried out on a FEI TECNAI F20ST transmission electron microscope operating at 200 kV at the Earth Science Department of the Università degli Studi di Milano, Italy. The microscope is equipped with a 1k CCD (Gatan 794MSC) camera for electron-diffraction data collection, a Nanomegas Spinningstar P020 device for precession electron diffraction and an EDAX EDS spectrometer for microanalysis.

ADT was carried out on a FEI TECNAI F30 ST transmission electron microscope working at 300 kV at the Institut for Physical Chemistry, Johannes Gutenberg University, Mainz, Germany. The microscope is equipped with a 1k CCD (Gatan 794MSC) camera, a Nanomegas Digistar device for precession electron diffraction and a FISCHIONE high-angle annular dark field (HAADF) detector for scanning transmission electron microscopy (STEM) imaging.

Zone-axis PED patterns with a large precession angle have been collected on a Philips CM30ST transmission electron microscope working at 300 kV at the CNRS Institute Néel Grenoble, France, equipped with a 1k CCD (Gatan 794MSC) camera for electron-diffraction data collection, and a Nanomegas Spinningstar P020 device for precession electron diffraction.

Simulations of the kinematical patterns have been carried out with the software *JEMS* written by P. Stadelmann.

The sample was prepared by separating from the matrix small fragments of yellow crystalline aggregates; these aggregates were ground in an agate mortar, suspended in isopropyl alcohol, and deposited on a copper holey carbon film grid for diffraction observations; for microanalysis, since

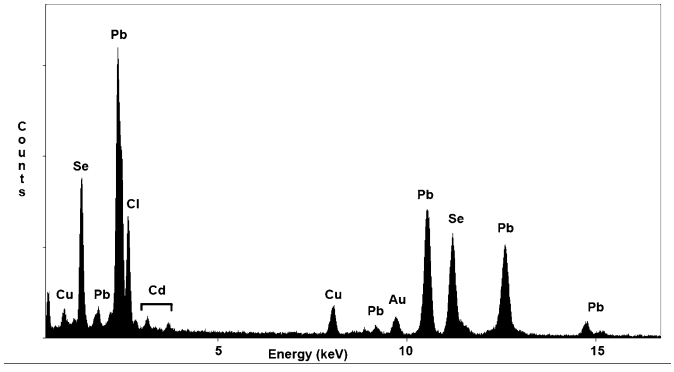

Figure 2
EDS spectrum of sarrabusite.

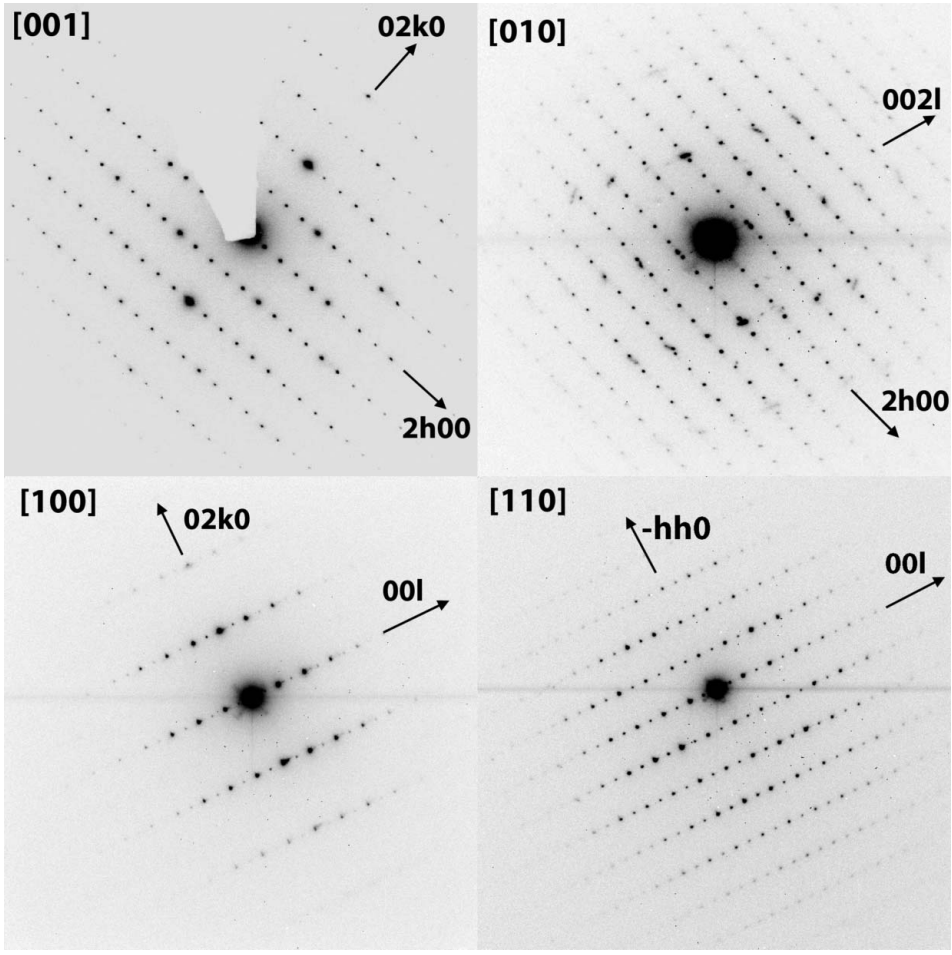

Figure 3
Selected-area electron-diffraction patterns collected on sarrabusite oriented in zone axes [001], [010], [100] and [110].

the mineral contains copper, a gold holey carbon film grid was used instead.

For the rendering of the crystal structure we have used the software *VESTA* (Momma & Izumi, 2008).

3. Results

3.1. Physical and chemical properties

The new mineral occurs as lemon yellow spherical aggregates of less than 100 μm in diameter of tabular crystals (<10 μm), showing a distinct cleavage (Fig. 1). The streak is white; the luster is vitreous. It is translucent and non-fluorescent either under SW or LW ultraviolet radiation. Hardness was not determined. Tenacity: brittle. The mean analytical results (average of seven analysed points) obtained at the electron microprobe are reported in Table 1.[1]

Starting from these data, the empirical formula (based on 16 anions) is $(Pb_{4.83}Cd_{0.20})_{\Sigma=5.03}Cu_{0.95}(Se_{3.94}S_{0.04})_{\Sigma=3.98}O_{11.83}Cl_{4.17}$; the simplified formula is $Pb_5CuCl_4(SeO_3)_4$ corresponding to: CuO 4.55, PbO 63.80, SeO_2 25.37, Cl 8.11, total 101.83, −O═Cl 1.83 total 100.00 (wt %). The calculated density is 6.011 g cm^{-3} (from the empirical formula and the unit-cell data). The presence of minor, but consistent amounts of cadmium is interesting: in order to provide the most reasonable chemical formula according to the chemical analysis, this element should replace lead rather than copper. This is in agreement with the ionic radii reported for Cd^{2+} by Shannon (1976) (0.95 and 1.10 Å in sixfold and eightfold coordination) and those reported by the same author for six-coordinated Cu^{2+} (0.73 Å) and eight-coordinated Pb^{2+} (1.29 Å).

The IR spectrum shows absorption bands at 810 and 738 cm^{-1} owing to the selenite ion. An approximate value for the index of refraction was obtained from the Brewster angle: n = 1.85 (2); the compatibility $1-(K_p/K_c)$ with Gladstone–Dale's estimate = 0.142 is poor. However, the accuracy of the measurement of the Brewster angle is low.

3.2. Determination of the crystal structure

Sarrabusite can be easily identified in the transmission electron microscope (TEM) owing to its characteristic microanalysis spectrum showing the presence of Pb, Se, Cu and Cl, and small amounts of Cd and Ca (Fig. 2); a very similar pattern was obtained using a SEM microanalysis (EDS mode, 20 kV, 10^{-11} A, 2 μm beam diameter). Sarrabusite is crystalline and it exhibits sharp selected-area electron-diffraction patterns (Fig. 3). From a set of such patterns, analysed with the program *QED* (Belletti *et al.*, 2000), a monoclinic *C*-centred unit cell with a = 24.7 (2), b = 5.50 (5), c = 14.2 (1) Å and β = 102 (1)° was deduced. The extinction conditions are compatible with space groups *Cc* or *C*2/*c*. The unit cell can be refined from X-ray powder-diffraction data (Table 2). A least-squares fit of these data using the program *UNITCELL* (Holland & Redfern, 1997) fully confirmed the results of electron diffraction and provided the following refined unit-cell parameters: a = 24.917 (3), b = 5.506 (1), c = 14.242 (2) Å, β = 101.77 (1)°, V = 1912.7 (3) Å^3. Two manual tilt series were collected: one without precession with α_{max} = 30° (61 patterns), and the other with the precession mode on

[1] Supplementary data for this paper are available from the IUCr electronic archives (Reference: DK5002). Services for accessing these data are described at the back of the journal.

Table 2
X-ray powder diffraction data of sarrabusite.

From left to right the columns report: the *hkl* indices of the reflection, the relative intensity (I_{rel}), the observed and the calculated *d* spacing (d_{obs}, d_{calc}).

hkl	I_{rel}	d_{obs} (Å)	d_{calc} (Å)
$\bar{2}02$	5	6.674	6.667
310	7	4.568	4.559
$\bar{4}02$	8	4.182	4.186
$\bar{5}\bar{1}1$	60	3.685	3.672
$\bar{3}12$	3	3.635	3.630
$\bar{4}04$	20	3.314	3.333
$\bar{8}02$	100	3.034	3.030
$\bar{5}14$	38	2.728	2.739
$\bar{8}04$	2	2.565	2.569
$\bar{1}\bar{1}5$	3	2.520	2.522
$\bar{9}\bar{1}2$	10	2.440	2.439
604	12	2.418	2.414
$\bar{4}06$	2	2.331	2.336
422	4	2.297	2.300
315	8	2.257	2.266
$\bar{2}06$	7	2.208	2.202
$\bar{4}24$	4	2.133	2.123
116	15	2.106	2.099
$\bar{7}14$	18	2.079	2.079
$\bar{8}\bar{2}1$	5	2.065	2.063
$\bar{8}\bar{2}2$	28	2.043	2.037
$\bar{9}\bar{1}5$	3	2.028	2.026
14,00	2	1.742	1.742
10,22	6	1.700	1.703
531	6	1.686	1.690

Calculated from the unit cell: $a = 24.917$ (3), $b = 5.506$ (1), $c = 14.242$ (2) Å, $\beta = 101.77$ (1)° obtained from least-squares refinement from the above data using the program *UNITCELL* (Holland & Redfern, 1997).

(precession angle 1°) within the maximum attainable tilt of the goniometer of $\alpha_{max} = 46°$ (93 PED patterns). The data were collected by positioning the smallest available SAED diaphragm on the thinnest edge of a 650 nm × 300 nm single crystal of sarrabusite (Fig. 4). The diffraction patterns were originally recorded in DM3 (GATAN) format and later converted into MRC format for further processing. The camera length calibration factor was transferred from original DM3 files and the tilt sequence was written into an MRC extended header. The MRC files obtained were processed using the *ADT*3D software package (Kolb *et al.*, 2011). For comparison, one ADT tilt series was collected using the automated acquisition module (STEM and nanodiffraction) on a crystal of similar size with precession on (precession angle 1°) and $\alpha_{max} = 60°$. The data collection time for the intensity acquisition runs, including crystal tracking and diffraction pattern exposure, was in the range of 1.5 h for both the manual and the automatic procedure.

The series without precession is used only for the unit-cell determination, since the positions of the spots do not suffer from indetermination due to the 1° precession movement. The primitive cell vectors were found first, then the corresponding vectors referred to the centered lattice were derived. Both manually collected (no precession and with precession) and ADT tilt series gave lattice unit-cell parameters close to the values obtained after refinement of X-ray powder diffraction data (Table 3). The accuracy of the length parameters depends on the electron-diffraction camera calibration: in this case they are systematically shorter by about 3%, with all manually and automated data. Electron-diffraction intensities were extracted from both manually and automated tilt series using the procedures reported by Mugnaioli *et al.* (2009). Fig. 5 shows views of the manually collected diffraction volume along the [100] and [001] directions: here the extinctions due to the *c*-type glide plane appear as rods of missing reflections along the *c** axis (Fig. 5*a*), and *C*-centering is evident in the [001] orientation (Fig. 5*b*). Both data sets confirm the possible space groups to be *C*2/*c* or *Cc*.

Structure solution was achieved using *SIR*2008, which is part of the IL MILIONE software package (Burla *et al.*, 2007), with both data sets. It was attempted first in the centrosymmetric space group *C*2/*c*; later on, the possibility of dealing with a lower symmetry *Cc* was also examined, but no significant improvement was obtained. The characteristics of the two data sets and some parameters relative to both structure solutions (agreement factors and average displacement parameters) can be found in Table 4. The reciprocal space coverage of ADT data is higher owing to the wider angular range of the data collection (120 *versus* 92°). The best solutions have an *R* factor of 0.329 (ADT) and 0.312 (manual collection): although such values are high for results of X-ray or neutron diffraction, they are considered as reasonable for electron diffraction (see also below). The highest potential peaks were assigned to 3 Pb, 2 Se, 1 Cu, 2 Cl and 6 O atoms in

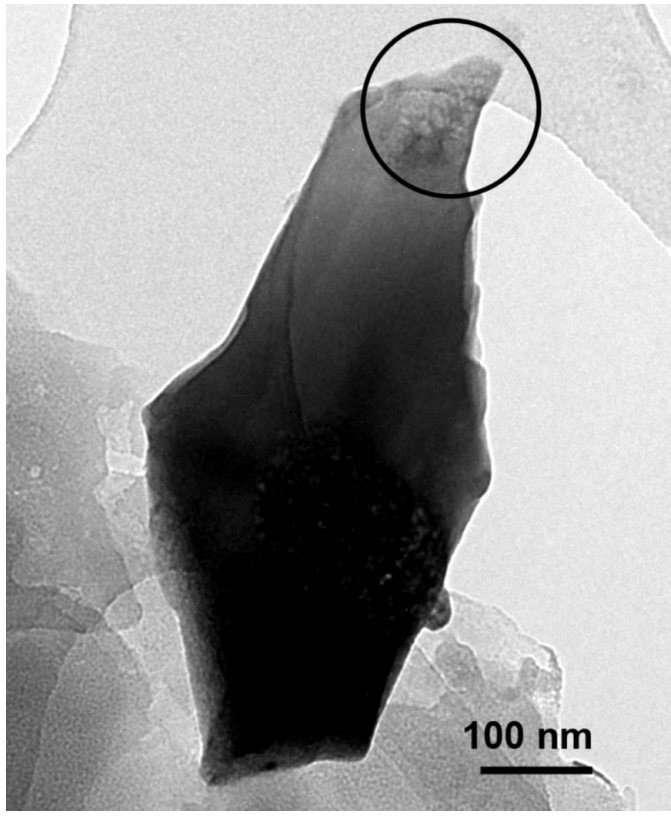

Figure 4
Bright field image of the sarrabusite crystal on which the manual diffraction tomography experiment has been carried out. On the top right a circle indicates the size and the location of the SAED diaphragm.

Table 3
Lattice cell parameters of sarrabusite determined by different methods.

Diffraction tomography data are reported as they are furnished by the *ADT*3D software. The parameters marked with asterisks have been kept fixed during the cell refinement to the value determined by the monoclinic symmetry.

	a (Å)	*b* (Å)	*c* (Å)	α (°)	β (°)	γ (°)
Zonal electron-diffraction data	24.7 (2)	5.50 (5)	14.2 (1)	90*	102 (1)	90*
X-ray powder refinement	24.917 (3)	5.506 (1)	14.242 (2)	90*	101.77 (1)	90*
Manual tomography (SAED)	24.199	5.499	13.826	89.576	101.902	90.372
Manual tomography (SAED + PED)	24.143	5.497	13.913	90.469	101.581	89.626
ADT	24.3997	5.4590	14.134	89.5773	102.8539	90.5560

Table 4
Details concerning the three-dimensional sets of reflection intensities, the average displacement parameter obtained with the Wilson plot and the agreement factor given by *SIR*2008 after the structure solution has been achieved.

We have reported the internal *R* value (R_{sym}) also calculated on *F* since it is the agreement factor usually reported by *SIR* that has been used in several previous publications (Gemmi *et al.*, 2003, 2010; Gemmi & Nicolopoulos, 2007).

	Automated	Manual
Input reflections	4872	2751
Independent input reflections	1515	915
$R_{sym}(I)$	0.204	0.255
$R_{sym}(F)$	0.134	0.167
Completeness (%)	81	65
B_{iso}/U_{iso}	1.88/0.0240	1.94/0.0245
Final residual value (*SIR*)	0.329	0.313
Final residual after refinement (*JANA*2006)	0.333	0.307

the asymmetric unit (Table 5); the lower peaks were interpreted as ghosts. After the assignment of the atomic species a chemically meaningful structure was obtained showing acceptable coordination polyhedra and the chemical formula $Pb_5CuCl_4(SeO_3)_4$ in agreement with that derived from the electron-microprobe analysis. The derived structural model is displayed in Fig. 6, and atomic (fractional) coordinates and isotropic displacement parameters are reported in Table 5. It is interesting to note that the high and low displacement parameters of atoms Cu1 and Pb3 are connected to the wrong automatic labeling done by *SIR* during the final Fourier recycling process. Cu1, in fact, is wrongly assigned by *SIR* as Pb and Pb3 as Cu, but the error can be easily detected on the basis of the coordination of the sites (see §4). We refined both models using *JANA*2006 (Petricek *et al.*, 2006), which is now modified to also treat electron data. The refinements are stable and converge but the final *R* values remain as high as those given by *SIR* (Table 4). The results of the refinements are displayed in Table 6 and the cation–anion distances are reported in Table 7. The errors in the atomic positions and distances are derived from the estimated standard deviations given by *JANA* but are obviously underestimated. The two refined models are closer to one another than the two solutions, indicating that the refinements try to converge to a unique model (compare Δ with $\Delta1$ in Tables 5 and 6). However, with *R* values as high as 0.30 we can conclude that because of the low quality of the electron-diffraction data due probably to residual dynamical effects and to the lack of a proper geometrical correction for PED, the final models are approximate.

4. Discussion

The main difference between the two models is in the displacement of some anions, since the positions of one Cl and three O atoms differ by more than 0.2 Å on passing from one to the other; while the cation positions are essentially the same, their maximum displacement is only 0.10 Å (for Se1). Such shifts slightly change the shape of some coordination polyhedra, but do not alter the nature of the structural model. This situation supports the validation of the structure, in view of the fact that the two data sets used in the structure solution were collected in two different ways, on two different crystals and with two different microscopes working at different high voltages. As further confirmation we collected several zone-axis patterns with a large precession angle (> 3°). These patterns are usually close to a kinematical condition (Gemmi & Nicolopoulos, 2007), thus they can be compared with a kinematical simulation calculated on the basis

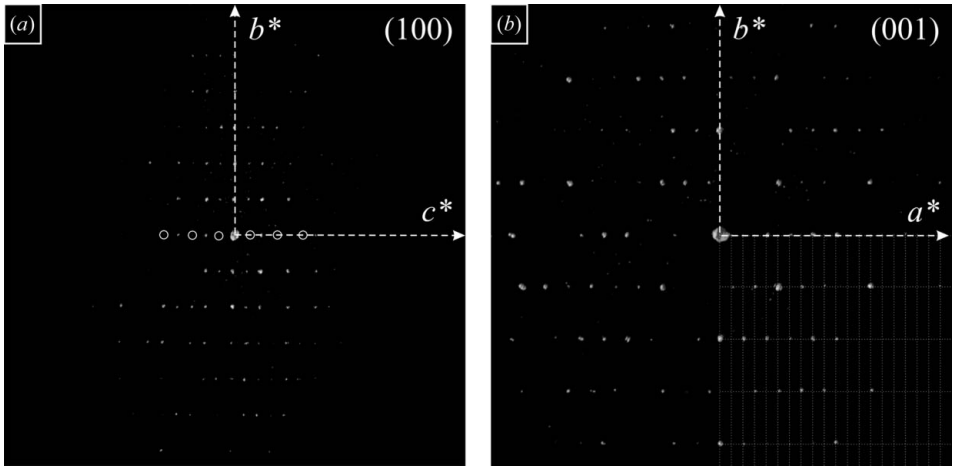

Figure 5
Views of ADT three-dimensional reconstructed reciprocal space along main directions.

Table 5
Atomic positions as given by *SIR*2008.

For each atom, the solutions obtained with manual (first row) and automated (second row) data are reported. Δ is the distance between the positions obtained with the two methods.

Atom	Wyckoff symbol	*x*	*y*	*z*	U_{iso}	Δ (Å)
Pb1	8*f*	0.1064	0.0632	0.1754	0.021	0.07
		0.1079	0.0585	0.1726		
Pb2	8*f*	0.2687	0.0142	0.3713	0.025	0.04
		0.2686	0.011	0.3687		
Pb3	4*e*	0	0.566	1/4	0.001	0.04
		0	0.559	1/4		
Se1	8*f*	0.1614	0.509	0.3315	0.010	0.15
		0.1660	0.497	0.328		
Se2	8*f*	0.0489	0.005	0.4115	0.021	0.09
		0.0453	0.006	0.410		
Cu1	4*b*	0	1/2	1/2	0.091	–
		0	1/2	1/2		
Cl1	8*f*	0.2960	0.486	0.451	0.037	0.20
		0.2911	0.502	0.458		
Cl2	8*f*	0.1230	0.523	0.538	0.040	0.49
		0.1029	0.514	0.529		
O1	8*f*	0.1812	0.740	0.268	0.005	0.11
		0.185	0.752	0.270		
O2	8*f*	0.0672	0.939	0.301	0.022	0.42
		0.057	0.876	0.300		
O3	8*f*	0.1871	0.233	0.286	0.030	0.34
		0.195	0.246	0.268		
O4	8*f*	0.0085	0.263	0.379	0.018	0.22
		0.011	0.234	0.391		
O5	8*f*	−0.0200	0.810	0.402	0.009	0.18
		−0.015	0.791	0.408		
O6	8*f*	0.1043	0.433	0.249	0.023	0.31
		0.0971	0.417	0.264		

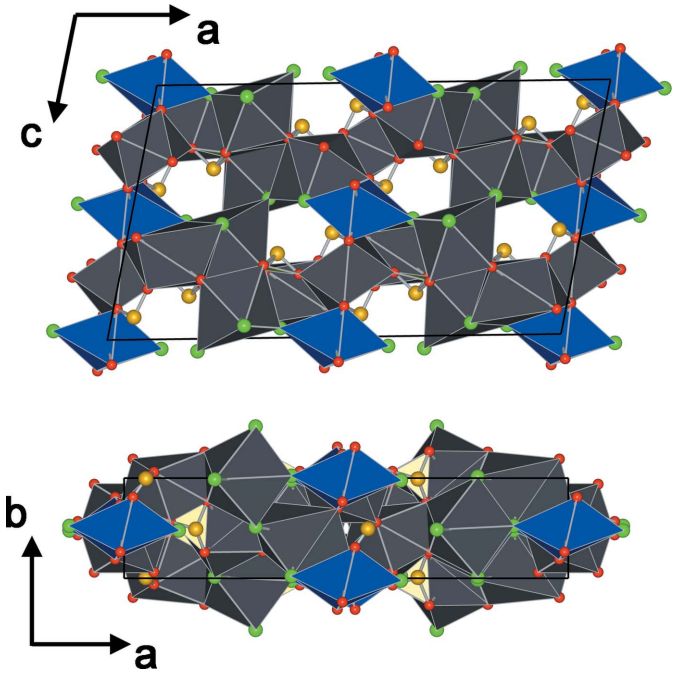

Figure 6
[010] and [001] projections of the sarrabusite structural model obtained with manually collected data. Grey polyhedra are centred by Pb, blue polyhedra are centred by Cu. Se atoms are yellow, O atoms are red and Cl atoms are green.

of the derived model. The comparison displayed in Fig. 7 for three main zone axes shows strong similarities.

The structure of sarrabusite contains three independent Pb atoms with eightfold coordination bonded to chlorine and/or oxygen (the Pb—O and Pb—Cl distances are in the ranges 2.32–3.04 and 2.82–3.42 Å; Table 7). The Pb atoms which are directly linked to both Cl and O (Pb1, Pb2) show a notably distorted coordination which can be described either as bicapped trigonal prismatic or as square antiprismatic. Pb3, which is coordinated only by oxygen, shows a more regular square-antiprismatic arrangement, similar to what happens for $PbTiO_3$ (Shirane *et al.*, 1956). Comparable coordinations can be found in other lead oxysalt halides or oxyhalides such as orlandiite $Pb_3Cl_4(SeO_3)\cdot H_2O$ (Demartin *et al.*, 2003), freedite $Pb_8Cu^{+}(AsO_3)_2O_3Cl_5$ (Pertlik, 1987), chloroxiphite $Pb_3Cu^{2+}Cl_2(OH)_2O_2$ (Finney *et al.*, 1977), diaboleite $Pb_2CuCl_2(OH)_4$ (Rouse, 1971). The square antiprisms observed in lead

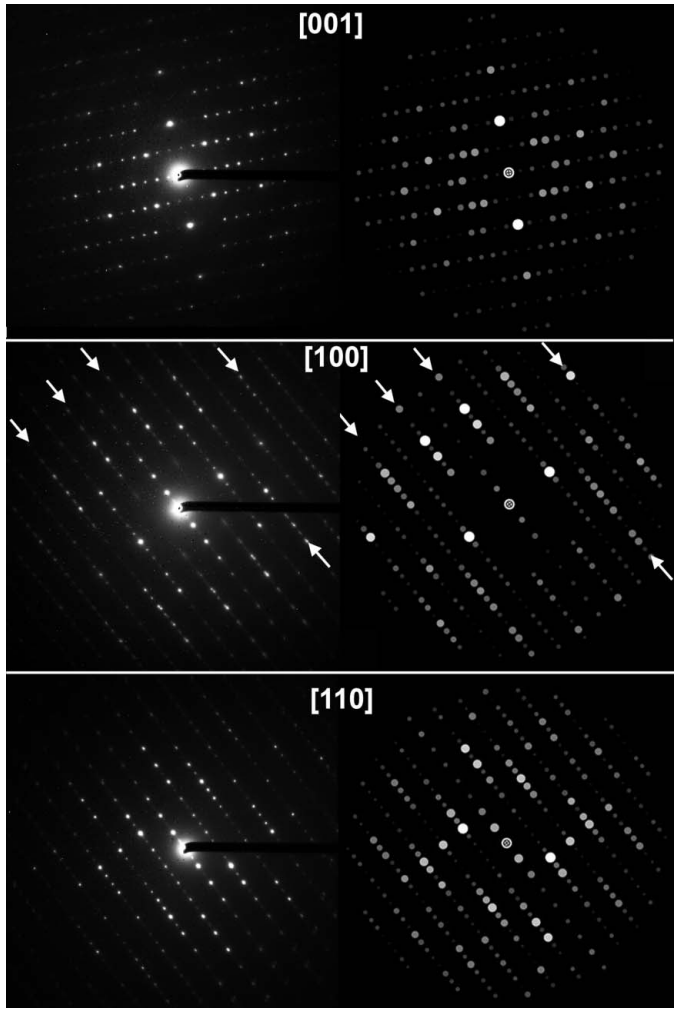

Figure 7
Precession electron-diffraction patterns (left) and kinematic simulations (right) of the [100], [001] and [110] zone axes. The simulations are calculated using the sarrabusite model obtained with *SIR*2008. The precession angles are 4° for [100] and 3.5° for [010] and [110]. The arrows in the [100] zone axis indicate reflection rows belonging to the first and higher-order Laue zones which arise since the *a* parameter is quite long.

Table 6
Atomic positions and isotropic displacement parameters refined with *JANA*2006.

For each position the refined valued obtained on manual and automated data are reported in the first and second row. We refined one displacement parameter for each atomic species. Δ1 is the shift of the atomic positions between the two refined models. Δ2 is the shift of the atomic positions between the original solution given by *SIR* and the refined model with *JANA*.

Atom	Wyckoff symbol	*x*	*y*	*z*	U_{iso}	Δ1 (Å)	Δ2 (Å)
Pb1	8*f*	0.1059 (3)	0.0639 (14)	0.1742 (8)	0.031 (3)	0.06	0.02
		0.1079 (2)	0.0627 (11)	0.1731 (4)	0.0333 (18)		0.02
Pb2	8*f*	0.2686 (3)	0.0123 (13)	0.3721 (9)	0.031 (3)	0.06	0.02
		0.2680 (3)	0.0103 (9)	0.3680 (4)	0.0333 (18)		0.02
Pb3	4*e*	0	0.562 (2)	0.25	0.031 (3)	0.04	0.02
		0	0.5542 (15)	0.25	0.0333 (18)		0.03
Se1	8*f*	0.1626 (6)	1.508 (2)	0.3293 (15)	0.019 (3)	0.10	0.05
		0.1649 (5)	0.4985 (16)	0.3261 (7)	0.027 (2)		0.04
Se2	8*f*	0.0461 (6)	0.003 (2)	0.4147 (15)	0.019 (3)	0.09	0.09
		0.0445 (5)	0.0084 (16)	0.4093 (7)	0.027 (2)		0.02
Cu1	4*b*	0	0.5	0.5	0.020 (5)	–	–
		0	0.5	0.5	0.036 (4)		–
Cl1	8*f*	0.2971 (11)	0.490 (4)	0.456 (3)	0.037 (5)	0.13	0.07
		0.2931 (10)	0.495 (3)	0.4599 (14)	0.035 (3)		0.07
Cl2	8*f*	0.1203 (11)	0.507 (4)	0.534 (3)	0.037 (5)	0.46	0.12
		0.1017 (9)	0.499 (3)	0.5323 (14)	0.035 (3)		0.10
O1	8*f*	0.1810 (15)	0.730 (7)	0.270 (4)	0.019 (4)	0.17	0.06
		0.1859 (12)	0.748 (5)	0.2764 (17)	0.026 (3)		0.09
O2	8*f*	0.0641 (15)	0.932 (7)	0.309 (4)	0.019 (4)	0.27	0.16
		0.0681 (11)	0.888 (5)	0.3061 (17)	0.026 (3)		0.28
O3	8*f*	0.1886 (14)	0.247 (7)	0.285 (4)	0.019 (4)	0.27	0.09
		0.1944 (12)	0.252 (5)	0.2709 (17)	0.026 (3)		0.06
O4	8*f*	0.0067 (15)	0.263 (6)	0.382 (4)	0.019 (4)	0.12	0.06
		0.0022 (12)	0.253 (5)	0.3816 (17)	0.026 (3)		0.25
O5	8*f*	−0.0173 (14)	0.807 (6)	0.404 (4)	0.019 (4)	0.16	0.07
		−0.0129 (12)	0.788 (5)	0.4094 (17)	0.026 (3)		0.06
O6	8*f*	0.1033 (15)	0.430 (7)	0.254 (4)	0.019 (4)	0.32	0.08
		0.0995 (12)	0.404 (5)	0.2716 (17)	0.026 (3)		0.13

Table 7
List of the cation–anion distances (in Å) calculated on the basis of the refined models of Table 6.

	Manual	Automated		Manual	Automated
Pb1—Cl1	3.36 (4)	3.42 (3)	Se1—O1	1.61 (5)	1.68 (3)
Pb1—Cl2	3.16 (3)	3.122 (19)	Se1—O3	1.74 (4)	1.80 (3)
Pb1—O1	2.77 (4)	2.79 (3)	Se1—O6	1.69 (4)	1.74 (3)
Pb1—O2	2.47 (5)	2.50 (3)			
Pb1—O3	2.54 (4)	2.54 (3)	Se2—O2	1.70 (6)	1.82 (3)
Pb1—O4	2.96 (4)	2.89 (3)	Se2—O4	1.75 (4)	1.71 (3)
Pb1—O5	2.67 (4)	2.85 (3)	Se2—O5	1.89 (4)	1.88 (3)
Pb1—O6	2.32 (4)	2.38 (3)			
			Cu1—Cl2	2.94 (3)	2.48 (2)
Pb2—Cl1	3.14 (3)	3.134 (17)	Cu1—Cl2	2.94 (3)	2.48 (2)
Pb2—Cl1	2.91 (3)	2.980 (17)	Cu1—O4	2.17 (5)	2.17 (3)
Pb2—Cl1	3.21 (4)	3.14 (2)	Cu1—O4	2.17 (5)	2.17 (3)
Pb2—Cl2	2.82 (3)	3.27 (2)	Cu1—O5	2.16 (4)	2.03 (3)
Pb2—O1	2.83 (4)	2.62 (3)	Cu1—O5	2.16 (4)	2.03 (3)
Pb2—O1	2.85 (5)	2.87 (3)			
Pb2—O3	2.48 (4)	2.45 (3)			
Pb2—O3	3.04 (5)	2.75 (3)			
Pb3—O2	2.62 (4)	2.52 (3)			
Pb3—O4	2.48 (5)	2.49 (3)			
Pb3—O5	2.69 (5)	2.69 (3)			
Pb3—O6	2.67 (4)	2.57 (3)			

oxychlorides with $PbCl_4O_4$ groups often exhibit two square basal faces, a smaller one formed by four O atoms and larger one formed by four Cl atoms (Finney *et al.*, 1977): such is exactly the situation of Pb2 in sarrabusite.

The Cu atom shows a bipyramidal (4 + 2) coordination with two Cl atoms at the vertices and four O atoms at the base of an elongated square bipyramid (Cu—O average 2.17/2.10 Å, Cu—Cl 2.94/2.48 Å for manual/ADT data models; Table 6); a similar arrangement of Cl and O atoms is observed for several copper oxychlorides such as chloroxiphite (Finney *et al.*, 1977) and diaboleite $Pb_2CuCl_2(OH)_4$ (Rouse, 1971), where, however, the basal O atoms are part of the hydroxyl groups.

The Se atoms display the characteristic threefold oxygen coordination of the SeO_3^{2-} anion, the three O atoms forming a base of a trigonal pyramid having the Se atom at the vertex.

All the cations are located on (010) planes close to $y = 0$ and $y = 1/2$. These cation layers are formed by straight chains of alternating edge-sharing CuO_4Cl_2 and $Pb3O_8$ polyhedra parallel to the *c* axis, which share corners laterally with two zigzag corner-sharing chains of $Pb1O_6Cl_2$ and $Pb2O_4Cl_4$ bicapped trigonal prisms. The blocks formed by zigzag and straight chains are linked together by the SeO_3^{2-} groups. The stacking of these layers is accomplished by superimposing the zigzag chains on top of one another (by sharing faces) and the straight chains on top of the SeO_3^{2-} groups bridging the zigzag chains (see Fig. 8).

Apart from the distortions of the polyhedra, the main difference between the two solutions lies in the position of the Cl2 atom located in between Pb2 and Cu1, that in the ADT solution is shifted towards Cu1 giving CuO_4Cl_2 with a short Cu—Cl (2.48 Å) distance compared with what occurs in similar compounds in the literature where normally at least one of the Cu—Cl distances is close to 3.0 Å (Finney *et al.*, 1977; Rouse, 1971). This can be an indication that Cl2 can be partially occupied by oxygen and in this case the atom moves toward Cu1, however, for any definite answer on structure details, like partial occupation or precise distances, better data are needed.

5. Conclusions

The sarrabusite structure is the first new mineral solved using manually collected electron-diffraction tomography data. The possibility of using a cheaper 'manual' version of ADT opens the possibility of wider applications of such a technique to electron microscopy. Although ADT, which uses STEM imaging for tracking the crystal position, remains the reference technique for beam-sensitive materials, in all other cases the 'manual' version can transform any standard TEM microscope into a true single-crystal electron diffractometer, provided that the tilt can be accurately controlled. These advantages especially apply to structural investigations of samples where, for different reasons, X-ray diffraction is not

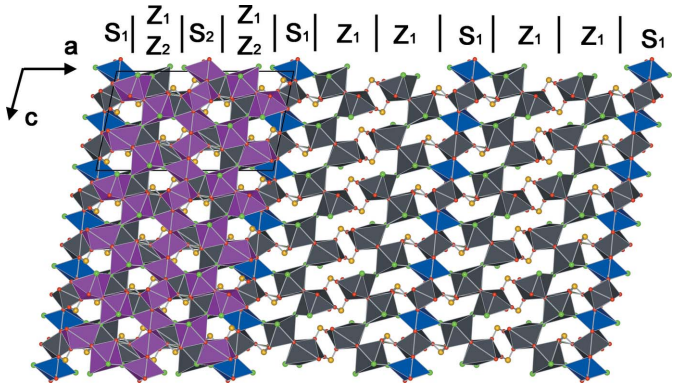

Figure 8
[010] projection of one cation layer (layer 1). The displayed region is 3 × 3 unit cells wide. The atom and polyhedra colors correspond to those used in Fig. 6. The purple polyhedra on the left are Pb and Cu polyhedra belonging to the above layer (layer 2) and are displayed to show the way in which the layers superimpose. The letters S_n and Z_n represent straight and zigzag chains (see text), while the subscript indicates the layer.

effective: typical examples are multiphase samples or samples where the amount of material is so scant that conventional X-ray diffraction is too weak for a proper structure analysis. The new mineral sarrabusite meets both these requirements.

Like orlandiite $Pb_3Cl_4(SeO_3)\cdot H_2O$, which is another species discovered in the same locality and often in close association, the new mineral sarrabusite is another lead selenite chloride, thereby confirming the existence of a nearly unique environment rich in both chlorine and selenium occurring at Baccu Locci.

MG acknowledges Holger Klein, Maria Bacia and Amelie Rageau for support during the TEM sessions at CRNS Institut Néel and for helpful discussions on precession electron diffraction.

References

Arndt, U. W. & Wonnacott, A. J. (1977). *The Rotation Method in Crystallography*. Amsterdam: North Holland.
Belletti, D., Calestani, G., Gemmi, M. & Migliori, A. (2000). *Ultramicroscopy*, **81**, 57–65.
Birkel, C. S., Mugnaioli, E., Gorelik, T., Kolb, U., Panthöfer, M. & Tremel, W. (2010). *J. Am. Chem. Soc.* **132**, 9881–9889.
Boullay, P., Dorcet, V., Pérez, O., Grygiel, C., Pellier, W., Mercey, B. & Hervieu, M. (2009). *Phys. Rev. B*, **79**, 184108.
Burla, M. C., Caliandro, R., Camalli, M., Carrozzini, B., Cascarano, G. L., De Caro, L., Giacovazzo, C., Polidori, G., Siliqi, D. & Spagna, R. (2007). *J. Appl. Cryst.* **40**, 609–613.
Campostrini, I. & Gramaccioli, C. M. (2001). *Neues Jahrb. Miner. Abh.* **177**, 37–59.
Campostrini, I., Gramaccioli, C. M. & Demartin, F. (1999). *Can. Mineral.* **37**, 1493–1498.
Cowley, J. M. (1968). *Prog. Mater. Sci.* **13**, 267–321.
Demartin, F., Gramaccioli, C. M. & Pilati, T. (2003). *Can. Mineral.* **41**, 1147–1153.
Dorset, L. D. (2006). *Z. Kristallogr.* **221**, 260–265.
Finney, J. J., Graeber, E. J., Rosenzweig, A. & Hamilton, R. D. (1977). *Mineral. Mag.* **41**, 357–361.
Gemmi, M., Klein, H., Rageau, A., Strobel, P. & Le Cras, F. (2010). *Acta Cryst.* B**66**, 60–68.
Gemmi, M. & Nicolopoulos, S. (2007). *Ultramicroscopy*, **107**, 483–494.
Gemmi, M., Zou, X. D., Hovmöller, S., Migliori, A., Vennström, M. & Andersson, Y. (2003). *Acta Cryst.* A**59**, 117–126.
Gjønnes, K. (1997). *Ultramicroscopy*, **69**, 1–11.
Gjønnes, J., Hansen, V., Berg, B. S., Runde, P., Cheng, Y. F., Gjønnes, K., Dorset, D. L. & Gilmore, C. J. (1998). *Acta Cryst.* A**54**, 306–319.
Gorelik, T. E., Stewart, A. A. & Kolb, U. (2011). *J. Microsc.* **224**, 325–331.
Hadermann, J., Abakumov, A. M., Tsirlin, A. A., Filonenko, V. P., Gonnissen, J., Tan, H., Verbeeck, J., Gemmi, M., Antipov, E. V. & Rosner, H. (2010). *Ultramicroscopy*, **110**, 881–890.
Holland, T. J. B. & Redfern, S. A. T. (1997). *Mineral. Mag.* **61**, 65–77.
Ji, G., Morniroli, J. P., Auchterlonie, G. J., Drennan, J. & Jacob, D. (2009). *Ultramicroscopy*, **109**, 1282–1294.
Jiang, J., Jorda, J. L., Yu, J., Baumes, L. A., Mugnaioli, E., Diaz-Cabanas, M. J., Kolb, U. & Corma, A. (2011). *Science*, **333**, 1131–1134.
Klein, H. (2011). *Acta Cryst.* A**67**, 303–309.
Kolb, U., Gorelik, T., Kübel, C., Otten, M. T. & Hubert, D. (2007). *Ultramicroscopy*, **107**, 507–513.
Kolb, U., Gorelik, T., Muganioli, E. & Stewart, A. (2010). *Polym. Rev.* **50**, 385–409.
Kolb, U., Gorelik, T. & Otten, M. T. (2008). *Ultramicroscopy*, **108**, 763–772.
Kolb, U., Schlitt, Heil, S. U., Schömer, E., Gorelik, T. E. & Mugnaioli, E. (2011). *ADT*3D. Institute of Physical Chemistry, Johannes Gutenberg University, Mainz, Germany.
Meshi, L., Ezersky, V., Kapush, D. & Grushko, B. (2010). *J. Alloys Compd.* **496**, 208–211.
Momma, K. & Izumi, F. (2008). *J. Appl. Cryst.* **41**, 653–658.
Morniroli, J. P., Stadelmann, P., Ji, G. & Nicolopoulos, S. (2010). *J. Microsc.* **237**, 511–515.
Mugnaioli, E., Gorelik, T. & Kolb, U. (2009). *Ultramicroscopy*, **109**, 758–765.
Nicolopoulos, S. & Weirich, T. (2007). *Ultramicroscopy*, **107**, 431–558.
Oleynikov, P., Hovmöller, S. & Zou, X. D. (2007). *Ultramicroscopy*, **107**, 523–533.
Own, C. S., Sinkler, W. & Marks, L. D. (2006). *Ultramicroscopy*, **106**, 114–122.
Palatinus, L., Klementová, M., Dřínek, V., Jarošová, M. & Petříček, V. (2011). *Inorg. Chem.* **50**, 3743–3751.
Pasero, M. & Perchiazzi, N. (1989). *Neues Jahrb. Miner. Monatsh.* **H12**, 551–556.
Pertlik, F. (1987). *Mineral. Petrol.* **36**, 85–92.
Petricek, V., Dusek, M. & Palatinus, L. (2006). *JANA*2006. Institute of Physics, Praha, Czech Republic.
Portillo, J., Rauch, E. F., Nicolopoulos, S., Gemmi, M. & Bultreys, D. (2010). *Mater. Sci. Forum*, **644**, 1–7.
Rouse, R. C. (1971). *Z. Kristallogr.* **134**, 69–80.
Rozhdestvenskaya, I., Mugnaioli, E., Czank, M., Dempmeier, W., Kolb, U., Reinholdt, A. & Weirich, T. (2010). *Mineral. Mag.* **74**, 159–177.
Shannon, R. D. (1976). *Acta Cryst.* A**32**, 751–767.
Shirane, G., Pepinsky, R. & Frazer, B. C. (1956). *Acta Cryst.* **9**, 131–140.
Sinkler, W. & Marks, L. D. (2010). *Z. Kristallogr.* **225**, 47–55.
Turner, P. S. & Cowley, J. M. (1969). *Acta Cryst.* A**25**, 475–481.
Vincent, R. & Midgley, P. A. (1994). *Ultramicroscopy*, **53**, 271–282.
Weirich, T. E., Portillo, J., Cox, G., Hibst, H. & Nicolopoulos, S. (2006). *Ultramicroscopy*, **106**, 164–175.
White, T. A., Eggeman, A. S. & Midgley, P. A. (2010). *Ultramicroscopy*, **110**, 763–770.
White, T. A., Moreno, M. S. & Midgley, P. A. (2010). *Z. Kristallogr.* **225**, 55–66.
Xie, D., Baerlocher, C. & McCusker, L. B. (2008). *J. Appl. Cryst.* **41**, 1115–1121.
Zhang, D., Oleynikov, P., Hovmöller, S. & Zou, X. (2010). *Z. Kristallogr.* **225**, 94–102.
Zou, X. D. & Hovmöller, S. (2008). *Acta Cryst.* A**64**, 149–160.